HHS Public Access

Author manuscript

Nat Methods. Author manuscript; available in PMC 2024 June 11.

Published in final edited form as:

Nat Methods. 2024 February ; 21(2): 342–352. doi:10.1038/s41592-023-02137-x.

Mapping Enzyme Activity in Living Systems by Real-Time Mid-Infrared Photothermal Imaging of Nitrile Chameleons

Hongjian He[1,2,#], **Jiaze Yin**[1,2,#], **Mingsheng Li**[1,2], **Chinmayee Vallabh Prabhu Dessai**[2,3], **Meihui Yi**[4], **Xinyan Teng**[2,5], **Meng Zhang**[2,3], **Yueming Li**[2,6], **Zhiyi Du**[2,5], **Bing Xu**[4], **Ji-Xin Cheng**[1,2,3,5]

[1]Department of Electrical and Computer Engineering, Boston University, Boston, MA 02215, USA.

[2]Photonics Center, Boston University, Boston, MA 02215, USA.

[3]Department of Biomedical Engineering, Boston University, Boston, MA 02215, USA.

[4]Department of Chemistry, Brandeis University, Waltham, MA 02453, USA

[5]Department of Chemistry, Boston University, Boston, MA 02215, USA.

[6]Department of Mechanical Engineering, Boston University, Boston, MA 02215, USA.

Abstract

Spatially mapping the activity of multiple enzymes in a living system is significant for elucidating enzymatic functions in health and connections to diseases. Here, we report the development of nitrile (C≡N)-tagged enzyme activity reporters, named nitrile chameleons for the peak shift between substrate and product. By real-time mid-infrared photothermal imaging of the enzymatic substrates and products at 300 nm resolution, our approach can map the activity distribution of different enzymes and quantitate the relative catalytic efficiency in living cancer cells, *C. elegans*, and brain tissues, enabling direct visualization of caspase-phosphatase interaction during apoptosis. Our method is generally applicable to a broad category of enzymes and heralds the potential of advancing discovery of targets for diagnosis and treatment.

Introduction

Enzymes, efficient and specific catalysts of a variety of biochemical reactions, play critical roles in literally all biological processes. Precise spatial and temporal regulation of enzyme activity is crucial to the successful operation of cellular machineries.[1] Thus, it is significant to spatially map and quantify the activity of enzymes, preferentially in living organisms for understanding the functions and roles of enzymes in health and disease. Notably, many

jxcheng@bu.edu .

[#]equal contributions

Author contributions: J.X.C. and H.H. deceived the concept. H.H. synthesized the probes, performed the experiments, and drafted the manuscript. J.Y. developed the laser-scanning MIP microscope. J.Y. and M.L. helped with MIP imaging. M.Y. and X.T. helped in the probe synthesis. M.Z. helped the culturing and MIP imaging of C. elegans. C.P.D., Y.L. and Z.D. helped with the extraction of mice brains, tissue sectioning and tissue imaging. B.X. provided material support on synthesis and intellectually contributed to the experiment designs.

Conflict of interest: The authors declare no conflict of interest.

biological events and signaling pathways, such as apoptosis[2], are accomplished by the cooperation of multiple enzyme species. Clearly, the attempts to map the activity of one kind of enzyme in one area of intertest (AOI) is insufficient to understand the cooperation among different enzymes in a complicated biological system. This gap urges the development of approaches that are capable of spatially profiling the activity of different enzymes in the same AOI at single cell level and in vivo for elucidating the links of multiple enzymes to life and pathophysiological processes.

Visualizing enzyme activity is largely performed by synthetic fluorogenic substrates.[3–5] However, current fluorogenic probes fail to provide spatial information because the water-soluble fluorophores tend to diffuse away from the reaction sites.[6] Recently, self-immobilizing fluorogenic reporters have been developed to locate enzyme activities in dynamic environments.[7] However, the covalent connection of bulky fluorophores to enzymes increase the risk of perturbing the function of the enzymes[8,9] and consequently disrupting the downstream signaling and cellular activity. Thus, the potential enzyme-silencing effects of self-immobilizing strategy diminish its application for mapping the activities of multiple enzymes in living systems.

A further development of fluorescent probes to profile enzyme activity in living organisms derive from in-situ enzymatic noncovalent synthesis (ENS)[10] of small molecules into non-diffusive nanostructures to allow the retention of fluorescent modalities at reaction sites.[11,12] Notably, the characteristics of fluorophores are critical to a successful mapping of enzyme activity via ENS-based fluorescent probes.[13–15] These filter criteria largely reduce the scope of fluorophore candidates. Given the broad-band emission spectrum, current research using this strategy mostly focuses on the mapping of one kind of enzyme in one AOI[16], which is barely enough to elucidate the cooperation between different enzymes in a biological process.

Beyond fluorescence, other technologies have been developed to map enzyme activity in cells and tissues[17], including magnetic resonance imaging (MRI) and mass spectrometry imaging (MSI)[18]. However, poor spatial resolution or inapplicability to living organisms significantly restrict these approaches towards high-resolution mapping of the activity of multiple enzymes in living subjects.

Addressing this challenge requires innovations in imaging systems and in chemistry. Here, we present a method for visualizing enzyme activities via real-time mid-infrared photothermal (MIP) imaging of a category of nitrile-tagged enzyme activity probes. The recently developed MIP microscope enables chemical imaging with submicron spatial resolution by sensing the photothermal effect induced by mid-infrared absorption with a visible light.[19,20] Importantly, such indirect measurement mitigates the huge water absorption issue and allows mid-infrared imaging in aqueous environment with high contrast.[21] The reported sample-scan MIP microscope needs a pixel dwell time ranging from 500 μs to 10 ms,[19,20] making it difficult to resolve the movements of living systems. To address these difficulties, we have developed a laser-scan MIP microscope with high speed and high sensitivity. In this new system, a synchronized laser scanning scheme is exploited

for high-speed imaging, enabling a pixel dwell time as short as a few microseconds.[22] These efforts collectively allow real-time MIP imaging of living systems.

While label-free MIP microscopy succeeds in visualizing the abundant cellular components[19,20], direct observation of specific enzymatic reactions in cells/tissues remains difficult because the MIP signals from products are immersed into the strong background from other biomolecules. To address this challenge, we synthesized a kind of nitrile-tagged bio-orthogonal enzyme activity probes. The vibration frequency of the nitrile group (C≡N) differs from those of endogenous functional groups, thus exhibiting unique IR absorbance in the cell-silent region.[23] The C≡N group has a relatively large infrared absorption cross-section and can serve as a sensitive photothermal reporter. Spectrally, the C≡N vibration is narrowband and tunable through chemical and physical approaches, enabling super-multiplexed detection.[24] Thus, adopting C≡N as a photothermal reporter of biochemical reaction is promising for bio-orthogonal detection of multiple enzyme activities in living systems. Here, we synthesized a series of nitrile-tagged enzyme activity probes, named nitrile chameleons. The probes exhibit reaction-activatable MIP spectral shifts of C≡N which signifies enzymatic reactions. These probes also perform in-situ ENS[10] for mapping enzyme activity.

Results

Performance of a laser-scanning MIP microscope

Figure 1a illustrates the principle of mid-infrared photothermal imaging. A mid-infrared light excites the chemical bond through vibrational transition. The vibrational energy is deposited into the sample which subsequently experiences a local temperature rise. The temperature escalation introduces several photothermal effects such as thermal expansion and refractive index alteration. Those changes influence the scattering of a visible probe, which is adopted as the photothermal signal.

Previous MIP microscopes relied on sample scan with a pixel dwell time of 500 μs or longer[21], which is insufficient in capturing the dynamics a living system. To increase the MIP imaging speed, we designed a laser-scan MIP microscope (Figure 1b) that provides a much faster pixel resolving speed on the order of a few microseconds (see methods). With such speed, it enables visualization of fast dynamics in real-time (20 Hz) at a small range with pixel counts under 25,000 (158×158). For providing high spatial resolution, counter-propagating geometry is applied to the microscope. Specifically, the visible beam is focused via a water immersion objective lens with 1.2 NA, while the infrared (IR) beam is focused by a reflective objective with 0.5 NA. The spatial resolution is characterized by imaging of PMMA particles with 200 nm diameter (Figure 1c). The resolution reached 300 nm, approaching the theoretical resolution of 276 nm estimated from point spread function (see supplementary information). The vertical resolution is determined to be 640 nm (Supplementary Figure 1), resulting in a voxel as a cube with lateral dimensions of 300 nm and axial dimensions of 640 nm. By synchronously scanning IR and visible beams with two pairs of galvo mirrors, a uniform field of view over 400 μm is reached (Figure 1d).

For live cell imaging, we optimized the IR excitation pulse width to maximize the signal to water background ratio. The photothermal dynamics of the water background is known to have a large decay constant (τ_B) due to the large heat capacity. The decay constant (τ_S) for the signal from organelles is usually smaller. We harness this difference to enhance the signal to background contrast by reducing the heating pulse duration τ (see supplementary information).[25] Experimentally, we compared the influence of heating pulse duration on the MIP contrast of a live cell at the protein channel (1553 cm^{-1}, amide II). Results show that a pulse duration of 50 ns provides the highest SBR with negligible photodamage (Figure 1e and Supplementary Figure 2). Thus, we demonstrated live cell MIP imaging at the protein channel (1553 cm^{-1}, Figure 1f and Supplementary Video 1) and kept the conditions for the following experiments unless specifically noted.

Nitrile-based enzymatic activity probes

We constructed two probes that selectively map the activity of phosphatase and caspase in living subjects because both phosphatase and caspase are critical to the survival and death of cells. Our phosphatase probe is generally applicable to different kinds of phosphatase, including alkaline phosphatase (ALP)[11], protein tyrosine phosphatase[26], acid phosphatase[27], and other types of phosphatases. The enzyme activity probes are comprised of an enzymatic substrate, a nitrile group (C≡N) as the reporter of enzymatic reaction, and a self-assembly moiety (Figure 2a and 2b). The nitrile-tagged probes for mapping the activity of caspase and phosphatases are named **Casp-CN(S)** and **Phos-CN(S)**, respectively. The enzymatic products are named **Casp-CN(P) and Phos-CN(P)**, respectively. The enzyme-catalyzed cleavage of the substrates alters the electronic donation from the para-position atoms (N or O), thus, significantly changing the electron density as well as the vibrational frequency of C≡N. Consequently, in the MIP spectra, the C≡N of enzymatic products are spectrally separated from those before enzymatic reactions. The MIP signal intensity of the C≡N of enzymatic products positively correlates with the level of enzyme activity. This reaction-activatable peak shift of C≡N not only reports the occurrence of enzymatic reactions, but also procures the exquisite detection specificity of enzymatic products via bio-orthogonal chemical imaging in the cell-silent region[28]. We further conjugated a self-assembly moiety to the probes (Figure 2a and 2b) to allow in situ ENS for conserving the products at the reaction sites. The ENS of the probes also amplify the imaging contrast via aggregation-enhanced responsiveness (AER)[29], a phenomenon likely caused by concentrating the targeted molecules within the volume of imaging. The amphiphilicity of the probes allows a solubility over 1 mM (see methods). We named this category of probes as nitrile chameleons because of the “spectral shift” of C≡N.

As shown in Figure 2c, the MIP spectra of the C≡N bond of **Casp-CN(S)** and **Casp-CN(P)** (50 mM, in DMSO) exhibit a sharp peak at 2225 and 2163 cm^{-1}, respectively, while **Phos-CN(S)** and **Phos-CN(P)** (50 mM, in DMSO) show narrow-band MIP spectrum of C≡N with a peak at 2215 and 2181 cm^{-1}, respectively (Figure 2d). These distinctive peaks of C≡N guarantee multi-color MIP imaging of the nitrile probes and the corresponding enzymatic products. Moreover, the MIP signal intensity of the C≡N bond in the enzymatic products is linearly proportional to the concentrations with a limit of detection (LOD) around 5 μM (Figure 2e, 2f and Supplementary Figure 3).

Next, we evaluated the enzymatic conversion efficiency of **Casp-CN(S)** by caspase-3 (active) and **Phos-CN(S)** by alkaline phosphatase (ALP) (Figure 2g and 2h). Time-course analysis of product formation reveals that the initial speed (v_0) is 0.23 $nmol^{-1}min^{-1}$ for **Casp-CN(S)** by caspase-3, and 0.29 $nmol^{-1}min^{-1}$ for **Phos-CN(S)** by ALP. The v_0 reduces slightly compared with that performed by standard substrates (Ac-DEVD-pNA, 0.33 nmol/min, and P-nitrophenyl phosphate, 0.53 nmol/min) in identical conditions (Supplementary Figure 4). No reaction occurred in the mixture of **Phos-CN(S)** or **Casp-CN(S)** with PBS, carboxylesterase-1 (CES-1), matrix metalloproteinase-2 (MMP-2), and proteinase K (Figure 2i and 2j), confirming the enzyme specificity for the reporters. Transmission electron microscopy (TEM) images of **Casp-CN(S)** and **Phos-CN(S)** (50 μM, in PBS) exhibit sparsely distributed small nanoparticles formed by the self-assembly of the probes (Figure 2k and 2l). Bulky nanofilaments formed by the self-assembly of products are observed after incubating the probes with corresponding enzymes for 1 hour (Figure 2k and 2l). Thioflavin T (ThT) was employed to examine the kinetics of nanofibril formation by the enzymatic products.[30] As shown in Figure 2m and 2n, ThT fluorescence surges within 10 seconds upon mixing with the enzymatic products (10 μM, PBS), suggesting a minimal nucleation phase and rapid nanoaggregate formation.[30] Thus, the enzymatic products settle near enzymes due to fast aggregation. Thermodynamically, the chemical potential of nanoaggregate formation positively links to monomer concentration.[31] Therefore, nanofibers predominantly develop near the enzymes because of the maximized product monomer concentration through local generation. However, according to Fick's law of diffusion, the distant product molecules are much less likely to assemble into nanofibers due to reduced concentration. These kinetic and thermodynamic factors ensure the nanoaggregates spatially associate with enzymes, and permits the spatial mapping of enzyme activities.

Real-time MIP imaging of enzyme activities in living cells

As shown in Figure 3a, the probes enter the cells and react with the corresponding enzymes, generating products that exhibit MIP signal at new wavenumbers. The MIP signal intensity from products is correlated with enzyme activity. The ENS of probes produce non-diffusive nanofilaments which uncover the reaction sites and enhance the imaging contrast by AER[29]. We first used this approach to map the activity of phosphatase in SJSA-1 cells, an osteosarcoma cell line with high phosphatase expression. A working concentration of 50 μM was chosen based on cytotoxicity assay (Supplementary Figure 5). All MIP images in the cell-silent window undergo a subtraction of water background as described in the methods unless specially mentioned. After the treatment of **Phos-CN(S)** (1 h), a pinpointed MIP spectrum in the silent window inside a cell (see methods for details on choosing the pinpointed area) exhibits a sharp peak at 2174 cm^{-1} arising from the C≡N of the dephosphorylated products (**Phos-CN(P)**), and a smaller peak at 2215 cm^{-1} originating from the C≡N of **Phos-CN(S)** (Figure 3b). This MIP spectrum identifies the optimal wavenumbers for imaging and validates the intracellular chemical components. The peaks of the C≡N inside cells shift compared to that in DMSO (Figure 2d), probably due to the Stark effect.[32] Live-cell MIP imaging at 1745 cm^{-1} reveals the profiles of lipid droplets in SJSA-1 cells (Figure 3c). Subsequent MIP images of the same cells at 2174 cm^{-1} show strong signal from **Phos-CN(P)**, while the intracellular MIP signal from **Phos-CN(S)** at 2215 cm^{-1} is weaker (Figure 3c and 3d). These results suggest an efficient cellular uptake

of the phosphatase activity probe, and that the phosphatases in SJSA-1 cells substantially convert **Phos-CN(S)** to **Phos-CN(P)**, disclosing a robust intracellular phosphatase activity.

Instead of a diffusive distribution, **Phos-CN(P)** exposes intricate subcellular structures varied by MIP intensity in the mapping (Figure 3c), indicating a heterogeneous biodistribution of phosphatase activity. To verify the non-diffusive property of nanofilaments in cells, we incubated cancer cells with **Phos-CN(S)** (1 hour) followed by fixation. We then sequentially captured two MIP images within the same field of view at a one-hour interval. The results (Supplementary Figure 6) show that little movement occurred during the one-hour interval, suggesting that the nanofilaments are highly immobile within cells. Although the Stokes-Einstein equation suggests high mobility for 100-nm particles in water, the nanofilaments formed by enzymatic products exhibited non-diffusive behaviors in the cells, likely due to the intertwining of nanofilaments, which constructs rigid nanonetworks that interact with cellular structures[33], thus restricting the mobility within the cellular environment. Such immobility ensures the spatial accuracy of enzyme activity mapping. However, the dissolved portion of **Phos-CN(S)** is hardly visible due to the lack of AER. Integrated MIP and widefield fluorescence imaging validate a good colocalization (Pearson's r=0.7, Supplementary Figure 7) between the MIP signal from **Phos-CN(P)** and the immunofluorescence from phosphatase antibodies (e.g., Anti-ALP), confirming the high spatial accuracy of mapping. As controls, we hardly observed MIP contrast in the cells without **Phos-CN(S)** treatment at 2174 cm^{-1} (Supplementary Figure 8A). These results collectively confirm successful mapping of phosphatase activity in living SJSA-1 cells by real-time MIP imaging of the nitrile chameleon.

Phosphatase inhibitor cocktails (PIC)-pretreated SJSA-1 cells incubated with **Phos-CN(S)** show a punctate distribution of **Phos-CN(P)** and **Phos-CN(S)** with much weaker MIP signals (Figure 3e and 3f) compared to the cells from inhibitor-free group (Figure 3c and 3d), which agrees with the phosphatase activity inhibition. These results validate that **Phos-CN(S)** can spatiotemporally unveil phosphatase activity change in cells. Given that the phosphatase level (e.g., ALP) in cells remains unchanged after PIC treatment (Supplementary Figure 9), the relative enzyme catalytic efficiency (k_{cat}/K_M) of phosphatase between the cells from PIC-pretreated and inhibitor-free groups can be approximately determined by the product-to-substrate ratio ([P]/[S], determined by the ratio of intracellular MIP intensity at 2174 cm^{-1} versus 2215 cm^{-1}) in cells (see supplementary information). The extent of PIC-induced inhibition on the k_{cat}/K_M of phosphatase in cells can be evaluated by this relative value. Statistically, the average [P]/[S] in PIC-pretreated cells is 2.5 times lower than the one in PIC-free group (Figure 3g), indicating that the average k_{cat}/K_M of the phosphatase in SJSA-1 cells decreases 60% through PIC treatment.

While the LOD of enzymatic products in DMSO approximate 5 μM, the minimum detectable concentration of the same molecules in cells, upon nanofilaments formation, is estimated to be around 600 nM (refer to supplementary information). Due to the uneven distribution of nanoaggregates in water, we used hyperspectral MIP images of **Phos-CN(P)** suspensions at concentration as low as 800 nM in PBS to substantiate this calculation. The peak of nitrile group is discernable in the spectrum obtained from the hyperspectral images (Supplementary Figure 10), affirming the sub-micromolar sensitivity of MIP in detecting

the nanoassemblies of enzymatic products. To further validate the high sensitivity of MIP imaging, we compared the MIP images to the fluorescence images of cells incubated **NBD-Phos-CN(S)**, a nitrobenzofurazan (NBD)-tagged **Phos-CN(S)** (Supplementary Scheme 1). Statistically, MIP images of C≡N at 2174 cm^{-1} (Supplementary Figure 11) and fluorescence images of NBD (Figure 3h) of the cancer cells incubated with **NBD-Phos-CN(S)** (50 μM, 1h) showed comparable signal to noise ratio (SNR) (Figure 3i). Here, SNR is the mean signal intensity in cells divided by that of blank area. Since C≡N and NBD exist in the molecule in a 1:1 ratio, this result indicates that the detection ability of C≡N by MIP resembles to that of NBD by fluorescence in cells. Furthermore, MIP imaging outperforms fluorescence imaging by a photobleaching-free property (Supplementary Figure 12), making it more suitable for observing continuous events in living systems.

Considering the high sensitivity and resistance to photobleaching, we conducted real-time monitoring of dephosphorylation reaction in cells by MIP imaging as **Phos-CN(S)** is introduced to the cells. As shown in Figure 3j, within 10 minutes of **Phos-CN(S)** addition, distinct puncta of dephosphorylated products were observed, indicating an efficient endocytosis-dependent cell entry and early endosomal dephosphorylation. Between 15 to 50 minutes, the MIP signal of enzymatic products appeared in other cellular regions with crooked-stripe patterns, indicating that **Phos-CN(S)** escaped from the endosomes and underwent dephosphorylation by the phosphatases in various cellular locations. The Nanoparticles formed by the amphiphilic nitrile chameleons may escape from endosomes through endosomal membrane disruption or perforation.[34] The variation in phosphatase activity patterns at different time points is attributed to the dynamic movements of cellular structures within live cells. As previously discussed, the nanofilaments intertwine with cellular structures, causing the nanofilaments to move along with these structures. Furthermore, we utilized **NBD-Phos-CN(S)** to study the cellular uptake mechanism of nitrile chameleons because NBD fluorescence cannot distinguish between substrate and product. As shown in Supplementary Figure 13, NBD fluorescence inside the cells was significantly reduced by ATP synthetase inhibitor (oligomycin, 5 μM), suggesting that the internalization of the probes occur through endocytosis.

Other than phosphatase, we profiled caspase-3/7 activity in live cancer cells. Doxorubicin (Dox) efficiently induces apoptosis in SJSA-1 cells for activating caspase-3/7 (Supplementary Figure 14). After the incubation with **Casp-CN(S)** (50 μM, 1 h), a pinpointed MIP spectrum inside a cell exhibits a sharp peak at 2163 cm^{-1} arising from the C≡N in **Casp-CN(P)** and a smaller peak originating from the C≡N in **Casp-CN(S)** at 2225 cm^{-1} (Figure 3k). This MIP spectrum provides the optimal wavenumbers for imaging and validates the intracellular chemical compositions. MIP imaging at 1745 cm^{-1} generates the map of lipid droplets in the cells (Figure 3l). MIP images of the Dox-pretreated SJSA-1 cells show intensive MIP signal from **Casp-CN(P)** at 2163 cm^{-1} and less signal from **Casp-CN(S)** at 2225 cm^{-1} with detailed spatial information (Figure 3l and 3m). These results indicate an efficient internalization of the caspase activity probe into cells, and a high caspase-3/7 activity in the Dox-pretreated SJSA-1 cells. Colocalization between **Phos-CN(S)** and **Phos-CN(P)** (Figure 3c), as well as **Casp-CN(S)** and **Casp-CN(P)** (Figure 3l) is observed, suggesting the coassembly between probes and products into non-

diffusive nanofilaments during ENS.[35–37] Tandem MIP and widefield fluorescence imaging validated a high spatial correlation between the MIP signal from **Casp-CN(P)** and the immunofluorescence from Caspase-3 (active) antibody (Pearson's r=0.72, Supplementary Figure 7). These results confirm a precise mapping of caspase-3/7 activity in apoptotic cells. While the nitrile chameleons are noncytotoxic (Supplementary Figure 5), incubating cancer cells with **Casp-CN(S)** showed a weak but non-zero MIP signal from **Casp-CN(P)** (Supplementary Figure 15a). Such signal disappeared upon the pretreatment of caspase-3/7 inhibitors (Supplementary Figure 15b). Together, these results indicate the presence of low-levels caspase-3/7 activity in non-apoptotic cells.[38–40]

The hydrophobic enzymatic products show little interaction with the plasma membrane or the lipid droplets (Figure 3c and 3l). Interestingly, the overall MIP intensity of C≡N increases along with the enzymatic cleavage in the cells (Figure 3c–f, 3l, Supplementary Figure 16), despite the same import efficiency of probe molecules into different the cell populations. This phenomenon can be explained by the assembly of products and substrates into non-diffusive nanofilaments after enzymatic cleavage, leading to an improved imaging detectability and cellular retention[41] of C≡N. The increased detectability arises from a higher molecular density in the imaging volume, enabling the targeted signals to stand out from background noise (Supplementary Figure 16a). Consequently, nanofiber formation corresponds to elevated C≡N accumulation and imaging detectability within cells, leading to higher MIP signal intensity. Incubating cancer cells with the control probes (Supplementary Scheme 2)[42,43] that are resistant to caspase-3/7 and phosphatase exhibited negligible MIP signal in cells at the wavenumber of the enzymatic products (Supplementary Figure 8b and 8c), supporting the accurate enzyme activity detection by MIP imaging of nitrile chameleons.

MIP imaging reveals caspase-phosphatase interaction

The MIP spectra of C≡N in **Phos-CN(P)** and **Casp-CN(P)** in cells appear as narrow bands at unique wavenumbers (Figure 3b and 3k), enabling multispectral imaging of these two enzymatic products. Thus, we simultaneously disclosed the activity distribution of phosphatase and caspase-3/7 in apoptotic cancer cells by MIP imaging of **Phos-CN(P)** and **Casp-CN(P)**, because the yield of enzymatic products aligns with the level and biodistribution of enzyme activities. As shown in Figure 4a, MIP imaging at 1553 cm^{-1} (amide II) and 1745 cm^{-1} displays the location and morphology of proteins and lipid droplets, respectively, in the Dox-pretreated SJSA-1 cells. After incubating the apoptotic cells with **Phos-CN(S)** and **Casp-CN(S)**, strong MIP signals from the C≡N of **Phos-CN(P)** and **Casp-CN(P)** with fine textures are observed in cells (Figure 4a), suggesting a high-level activity of phosphatase and caspase-3/7 in the cells. The merge channel and colocalization analysis confirms a weak spatial correlation between the MIP signals from **Phos-CN(P)** and **Casp-CN(P)** (Pearson's r=0.42, Figure 4b), validating that MIP imaging of nitrile chameleons not only visualizes, but also spatially and spectrally distinguishes the activity distribution of different enzymes.

Interestingly, while the activity maps of phosphatase and caspase-3/7 are mostly independent, sporadic coexistences were observed in the cells (Figure 4c). The overlapping

between the activity maps of phosphatase and caspase-3/7, while infrequent, suggests the coexistence and co-assembly of their enzymatic products in certain areas within the cells. Since the MIP signal of enzymatic products spatially corresponds to the biodistribution of enzyme activities, such overlapping indicates that the activity of caspase-3/7 and phosphatase are spatially close in some areas of the cells, suggesting potential phosphatase-caspase interactions in apoptosis. It is reported that PTEN[44] and PTP-PEST[45] are potential substrates of caspase-3. Importantly, the caspase-3-catalyzed cleavage of PTP-PEST increases the catalytic activity of PTP-PEST.[45] Notably, in the activity map of phosphatase and caspase-3/7, areas with colocalization generally exhibit stronger MIP signal from **Phos-CN(P)** than the ambient, as revealed by the intensity plots along the arrows (Figure 4d). This indicates a higher phosphatase activity in the sites that are coupled with caspase 3/7 activity. Statistically, the activity level of phosphatase in SJSA-1 cell population positively associated with that of caspase-3/7 (Figure 4e). These results indicate potential caspase-phosphatase interactions during apoptosis, probably through enzymatic cleavage with some phosphatase as the substrates of caspase. Such interactions appear to influence the activity of phosphatases in cells. Nevertheless, it's important to note that the alterations in phosphatase activity during apoptosis may occur through many other biochemical processes within the apoptosis signaling pathway, rather than being solely attributed to the direct processing of phosphatases by caspase-3/7.

To further confirm the interaction between phosphatase and caspase-3/7 during apoptosis, we imaged the intracellular distribution of caspase-3 proteins (full-length and cleaved) and the activity map of phosphatase in Dox-pretreated cancer cells in the presence and absence of a caspase-3 inhibitor (Z-DEVD-FMK, 10 μM). In this study, caspase-3 protein in the cancer cells was visualized by immunofluorescence staining using a confocal fluorescence microscope. To locate the phosphatase activity alongside caspase-3 protein via confocal fluorescence microscopy, we incubated cancer cells with **NBD-Phos-CN(S)** and located phosphatase activity through NBD fluorescence. This approach, known as fluorescence ENS, has been widely used to expose the location of enzyme activity[11,46,47]. The results demonstrated that cancer cells in the caspase inhibitor-treated group exhibited a significantly reduced spatial overlapping frequency between the phosphatase activity map and the caspase-3 proteins than the cells in the inhibitor-free group (Supplementary Figure 17). This supports our hypothesis that caspase-3 and some phosphatases interact in the colocalized regions through enzymatic cleavage, with some phosphatase acting as the substrate of caspase-3. Thus, the simultaneous mapping of phosphatase and caspase-3/7 activity probably localizes the caspase-mediated cleavage of phosphatase, likely PTP-PEST[41], in the apoptotic SJSA-1 cells. In addition to SJSA-1, we observed a similar scenario in MIA PaCa-2 (Supplementary Figure 18). Furthermore, a slight inhibition of phosphatase activity rescued cancer cells from Dox-induced cell death (Figure 4f), strengthening the notion that phosphatase activity is crucial in apoptosis signaling[48–51].

Multicolor MIP imaging of enzyme activities in *C. elegans* and brain tissues

We explored enzyme activity mapping in *C. elegans* and brain tissues via MIP imaging of the nitrile chameleons. After incubating **Phos-CN(S)** with *C. elegans*, real-time MIP imaging at 1745 and 2174 cm^{-1} revealed the biodistribution of lipid droplets and **Phos-**

CN(P) which exposed the phosphatase activity profile in *C. elegans* (Figure 5a). While *C. elegans* lack ALP, the intensive MIP signal from the C≡N of **Phos-CN(P)** at 2174 cm^{-1} and a weaker one from **Phos-CN(S)** at 2215 cm^{-1} confirm an efficient enzymatic conversion (Figure 5a and 5b), suggesting a high activity from other phosphatase isoenzymes, such as PTP, in *C. elegans*.[52] As controls, MIP contrast is hardly observed in the *C. elegans* without nitrile chameleon treatment (Supplementary Figure 19). PIC significantly reduces the phosphatase activity in *C. elegans*, as revealed by the weaker MIP signal from **Phos-CN(P) and Phos-CN(S)** (Figure 5c and 5d). To avoid cell death due to the cytotoxicity of PIC, the PIC concentration we employed might not completely deplete phosphatase activity in cells and *C. elegans*, resulting in the remnant of some phosphatase activity. The average [P]/[S] obtained from the PIC-treated *C. elegans* versus one from the inhibitor-free group suggests a 54% decrease in the catalytic efficiency (k_{cat}/K_M) of the phosphatase (Figure 5e) in *C. elegans* via PIC treatment. Although the caspase (e. g. CED-3) of *C. elegans* may differ from the one of a human, DEVD works as the substrate.[53] We exposed *C. elegans* to UV radiation to induce apoptosis for caspase activation.[54] After incubating the UV-irradiated *C. elegans* with **Casp-CN(S)**, real-time MIP imaging at 2163 cm^{-1} reveals the activity profile of the caspase in *C. elegans* (Figure 5f). The strong MIP signal from **Casp-CN(P)** and the lower signal from **Casp-CN(S)** at 2223 cm^{-1} confirm a high caspase activity in the UV-treated *C. elegans* (Figure 5f and 5g). Conversely, faint MIP signals from **Casp-CN(P)** and **Casp-CN(S)** were observed in the UV-free *C. elegans* (Supplementary Figure 20), indicating the existence of a weak caspase activity background in *C. elegans*. We further reconstructed the 3D activity profiles of phosphatase and caspase in the nematode (Figure 5h and 5i and Supplementary Video 2 and 3). Besides visualizing the enzyme activity individually, we concurrently mapped the activity of phosphatase and caspase in *C. elegans* through incubating the UV-irradiated C. elegans with nitrile chameleons followed by MIP imaging (Figure 5j). The merge channel and colocalization analysis show a poor overlapping between the MIP signals from **Phos-CN(P)** and **Casp-CN(P)** (Pearson's r=0.23, Figure 5k), confirming the identification and differentiation of the activity profiles of diverse enzymes in C. elegans by MIP imaging of nitrile chameleons.

We further concurrently mapped the activity of phosphatase and caspase-3/7 in sections of mouse brains. Caspase-3/7 in fresh mouse brains were activated through an ex vivo incubation with Dox (1 μM, 24 h), simulating chemotherapy-induced neurotoxicity. After incubating the Dox-treated tissues with nitrile chameleons, MIP imaging produced clear activity maps of phosphatase and caspase-3/7 in the unfixed tissue sections of cerebral cortex (Figure 5l and 5m). MIP images of the phosphatase activity map in the brain slices resemble the pattern of phosphatase histochemistry, which reveals the dense network of capillaries in the cortical mantle.[55] The merged channel and colocalization analysis revealed a low spatial overlapping between **Phos-CN(P)** and **Casp-CN(P)** (Pearson's r=0.34, Figure 5m). This supports the capability to identify and differentiate the activity distribution of various enzymes in the cerebral cortex via MIP imaging of nitrile chameleons. In tissues without the treatment of nitrile chameleons serving as controls, little MIP contrast of C≡N is shown (Supplementary Figure 21).

Discussion

We have reported a broadly applicable approach to acquire new perceptions on the functions of multiple enzymes in biological events, health regulation, and pathological developments. The holistic comprehension in the characters of multiple enzymes will greatly promote the discovery of potential drug targets for diagnostic and therapeutic applications.

Our approach addresses the challenge of visualizing the activities of multiple types of enzymes simultaneously within live cells. Prior fluorescence-based studies[56–59] focused on imaging individual enzymes in separate fields of view and led to an insufficient understanding of the interactions between different types of enzymes within the same cell or organism. Here, the development of a laser-scan MIP microscope and the synthesis of nitrile probes outperforms traditional enzyme activity imaging approaches by mapping the activities of multiple enzymes in the same field of view inside of a live cell. Moreover, our approach endows the comparison of the catalytic efficiency of specific enzymes between different cell populations, exceling beyond conventional off-on probes[3,60] for imaging enzyme activity. An intriguing finding is the visualization of caspase-phosphatase interaction during apoptosis inside cancer cells. As multiple enzymes may share the same substrate, further development of probes with high enzyme specificity is crucial for understanding the function of a particular enzyme in various biological processes and diseases. Developing a more precise mathematical model for k_{cat}/K_M quantitation is another worthwhile future endeavor.

While we focus on caspase and phosphatase in this study, activity mapping of a broad category of enzyme species can be done by developing more spectrally resolvable enzymatic reaction reporters[24,28,61] (Supplementary Scheme 3). Additionally, enzyme activity profiling in other tissues, such as a tumor, is worth exploration. Furthermore, the nitrile chameleon concept, namely the reaction-activable spectral shift of C≡N, can be extended for detecting numerous cellular activities, including pH, reactive oxygen species, membrane potential, and post-translational modification.

Methods

Materials:

RPMI-1640 culture medium was purchased from Thermofisher Scientific. RPMI 1640 culture medium for SJSA-1 cell (ATCC, CRL-2098) culturing was supplied by 10% (vol/vol) FBS and 1% (vol/vol) penicillin/streptomycin to the medium. DMEM culture medium was purchased from Thermofisher Scientific. DMEM culture medium for MIA PaCa-2 (ATCC, CRM-CRL-1420) cell culturing was supplied by 10% (vol/vol) FBS and 1% (vol/vol) penicillin/streptomycin to the medium. Nematode Growth Medium (NGM) for preparing C. elegans suspension was purchased from Fisher Scientific. Phosphatase Inhibitor Cocktail II (PIC) was purchased from Sigma Aldrich. Caspase-3/7 inhibitor Z-DEVD-FMK was purchased from Sigma Aldrich. All amino acid derivatives involved in the synthesis were purchased from Fisher Scientific. N, N’-diisopropylethylamine (DIEA) and O-(1H-Benzotriazol-1-yl)-N,N,N’,N’-tetramethyluronium hexafluorophosphate (HBTU) were purchased from Fisher Scientific. Human recombinant active caspase 3 was purchased

from Abcam (ab52101), and alkaline phosphatase was purchased from Sigma Aldrich (10713023001). Caspase 3 (cleaved and full length) antibody was purchased from Cell Signaling (# 9662). All reagents and solvents were used as received without further purification unless otherwise stated.

Laser-scan MIP microscope:

The laser-scan MIP microscope is built on an inverted microscope frame (IX73, Olympus). The visible probe is provided by a continuous-wave 532 nm laser (Samba, HUBNER photonics). The mid-infrared pump is provided by a pulsed quantum cascade laser (MIRcat 2400, Daylight Solutions) tunable from 900 cm^{-1} to 2300 cm^{-1}. The visible beam is scanned by a galvo mirror with 3 mm aperture (Saturn 1B, ScannerMax) and focused with a water immersion objective lens (1.2NA, 60X, Olympus). The IR beam is synchronously scanned with another pair of galvo mirrors (GVS001, Thorlabs) and focused on the same spot with a reflective objective (0.5NA, 40X, Thorlabs). For IR beam scanning, reflective conjugation with two concave mirrors is used for removing the chromatic aberration. Probe photonics are collected in both forward and backward directions. Their intensity is sensed by a silicon photodiode (DET100A, Thorlabs) connected with low-noise amplifier (SA230, NF cooperation). The amplifier signal is then sent to a lock-in amplifier (HF2LI, Zurich) for MIP signal demodulation. The microscope is controlled by LabView 2020.

Synthesis of nitrile probes:

The synthesis of self-assembly moiety was based on solid-phase peptide synthesis (SPPS). All probes were purified by Water Agilent 1100 HPLC system, equipped with an Xterra C18 RP column. Details of the probe synthesis can be found in the supplementary information.

Transmission electron microscopy (TEM):

TEM images were taken on Morgagni 268 transmission electron microscope using negative staining. Samples were dropped on copper grids and dried by vacuum. Uranyl acetate (1 wt%, pH 4.5) was used to stain the samples 3 times followed by washing using distilled water. Images were taken by lab members who were properly trained.

Limit of Detection (LOD):

The LOD in this work is defined as the concentration at which the MIP signal from the molecule equals to 3 times of the standard deviation of background noise. A drop of solutions of **Casp-CN(P)** and **Phos-CN(P)** dissolved in DMSO at different concentrations was put on a CaF2 crystal glass and put under our MIP microscope. We focused on the center of the drop. We obtained the MIP spectra of **Casp-CN(P)** and **Phos-CN(P)** dissolved in DMSO at different concentrations in cell-silence window until the MIP signal intensity at the peaks from the molecules was equal to 3 times of the standard deviation of background noise. The lock-in integration time used for measurement is set to 50 milliseconds.

In vitro time-course monitoring of product formation:

The in vitro time-course formation of enzymatic products from standard substrates was done by following the manufacture’s protocol. Briefly, colorimetric substrates Ac-DEVD-pNA

(100 μM) and pNPP (200 μM) were mixed with active caspase 3 (25 U/mL) and ALP (0.5 U/mL), respectively, at room temperature in PBS buffer. The UV absorbance at 405 nm was monitored over time by a UV-Vis spectrometer. Standard curves of enzymatic products were constructed to determine the product concentrations according to UV absorbance (Supplementary Figure 4).

The in vitro time-course formation of enzymatic products from nitrile chameleons were done in a similar way. Briefly, **Casp-CN(S)** (100 μM) and **Phos-CN(S)** (200 μM) were mixed with active caspase 3 (25 U/mL) and ALP (0.5 U/mL), respectively, at room temperature in PBS buffer. The UV absorbance of **Casp-CN(S)** (100 μM) mixed with caspase 3 was monitored at 325 nm over time by a UV-Vis spectrometer. The UV absorbance of **Phos-CN(S)** (200 μM) mixed with ALP was monitored at 340 nm over time by a UV-Vis spectrometer. Standard curves of enzymatic products were constructed to determine the product concentrations according to UV absorbance (Supplementary Figure 4).

For the experiments to determine off-targeting effects, probes were mixed with CES-1 (1 mg/ml), MMP-2 (10 U/mL), proteinase k (0.1 mg/mL), ALP (0.5 U/mL), and caspase 3 (25 U/ml), respectively, in PBS at room temperature. The UV absorbance of the mixtures were monitored over time by a UV-Vis spectrometer.

Sample preparation:

For MIP imaging of live cells, SJSA-1 and MIA PaCa-2 cells were firstly seeded on CaF_2 crystal substrates with a density of 1×10^5/mL with 2 mL culture medium for overnight at 37 °C and 5% CO_2. After cell attachment, cells were pretreated by conditions of interest. For examples PBS (control), Dox (2 μM, 24 h), and Phosphatase Inhibitor Cocktail II (0.25 μL in 1 mL medium, 24 h). After the treatment, cells were incubated with **Phos-CN(S)** (50 μM, 1 h) for phosphatase activity mapping, or **Casp-CN(S)** (50 μM, 1 h) for caspase activity mapping. Cells were then washed by PBS 3 times, and sandwiched over a cover glass, followed by MIP imaging. For concurrent mapping the activity of two enzymes, solution of **Phos-CN(S)** (100 μM) and **Phos-CN(S)** (100 μM) were mixed at 1:1 ratio. Cells (2 μM Dox treated) were incubated with the mixture of probes (1 h), then washed by PBS 3 times, and sandwiched over a cover glass, followed by MIP imaging. IR frequency: 1 MHz; IR power: 5–18 mW; Probe beam: 20 mW; IR pulse width: 50 ns; Pixel dwell time: 4 μs.

For the optimization of laser pulse width, SJSA-1 cells were firstly seeded on CaF_2 crystal substrates with a density of 1×10^5/mL with 2 mL culture medium for overnight at 37 °C and 5% CO_2. After cell attachment, cells were fixed by 4% formaldehyde to avoid shrinkage caused by heat damage while using long laser pulse width.

For MIP imaging of live *C. elegans*, *C. elegans* (daf-2 (e1370) mutant strain, caenorhabditis genetics center) were grown at 20°C on NGM agar seeded with *Escherichia coli* OP50 by PBS washing. The *C. elegans* and *e. coli* suspension were centrifuged at 400 × g for 30 s to separate *C. elegans* from *e. coli*. The *C. elegans* were resuspended in NGM followed by the treatment of conditions of interest. For example, PBS (control), UV exposure (254 nm, until the movement of most *C. elegans* slow down) using a UV Stratalinker 2400, and PIC

II treatment (1 μL PIC in 1 mL). After that, the nitrile chameleons (50 μM) were mixed with *C. elegans* in NGM and incubated for one hour. The *C. elegans* were then washed by centrifuged at 400 × g in PBS 3 times and sandwiched between CaF_2 crystal substrate and cover glass for MIP imaging.

For the 3D reconstruction of enzyme activity map in *C. elegans*, wild-type *C. elegans* were grown at 20°C on NGM agar seeded with *Escherichia coli* OP50 by PBS washing. The *C. elegans* and *e. coli* suspension were centrifuged at 400 × g for 30 s to separate *C. elegans* from *e. coli*. The *C. elegans* were resuspended in NGM followed by the treatment of conditions of interest. The *C elegans* were then fixed by 4% formaldehyde to prevent movement during the 3D reconstruction.

For MIP imaging of the cerebral cortex, two nude mice (Jackson lab Cat#JAX:00555, female, 4 weeks) were anesthetized by isoflurane. For all animal experiments, mice were housed at 21 °C-23 °C with a 12/12 dark/light cycle. The humidity of the housing environment is 35%. The mice were checked with a tail pinch and were quickly decapitated. The scalps and skulls were opened with scissors and the brains were carefully removed. The brains were placed in PBS at room temperature and were washed with PBS. The brain tissues were then cultured in 49 mL Hibernate-E Medium + 0.25 mL Gentamicin + 1 mL B-27 Plus Supplement + 50 uL Amphotericin B at 37 °C. Dox was then added into the medium to a final concentration of 1 μM. The brains were further incubated for 24 h. The brains were transferred to new culture medium containing **Casp-CN(S)** and **Phos-CN(S)** (50 μM) for 4 hours at 37 °C. After treatment, the tissue was sliced to coronal sections with a thickness of 100 μm using an Oscillating Tissue Slicer (OST-4500, Electron Microscopy Sciences). Brain slices were gently transferred by a brush and sandwiched between a CaF_2 substrate and a cover glass for MIP imaging. The protocol of animal experiments was approved by BU IACUC (PROTO201800534).

Immunofluorescence imaging:

All samples were fixed using 4% formalin in PBS pH 7.4 for 10 min at room temperature. Then, the samples were washed by PBS for 3 times, 5 min each, to remove formalin residues. The samples were permeabilized for 10 min with PBS containing 0.25% Triton X-100. Samples were Washed in PBS three times for 5 min. Samples were incubated with 1% BSA, 22.52 mg/mL glycine in PBST (PBS+ 0.1% Tween 20) for 30 min to block unspecific binding of the antibodies. Then, samples were incubated in 1000X diluted antibody (Anti-Alkaline Phosphatase antibody, Abcam, ab354; Anti-Cleaved Caspase-3 antibody, Abcam, ab2302; Anti-Caspase-3 antibody, full length and cleaved, cell signaling #9662) in 1% BSA in PBST in a humidified chamber for overnight at 4°C. After that, wash the cells three times in PBS, 5 min each wash. Incubate cells with 500X diluted secondary antibody (Goat anti-rabbit IgG labeled with Alexa-532, Thermofisher Scientific, Catalog # A-11009) in 1% BSA for 1 h at room temperature in the dark. Decant the secondary antibody solution and wash three times with PBS for 5 min each in the dark. Now the samples are ready for imaging.

Acquisition of pinpointed MIP spectra:

To determine the area in cells to get pinpointed MIP spectrum, MIP images of the cells were initially captured at the wavenumbers of C≡N of enzymatic products derived from their corresponding DMSO solutions (2205 and 2221 cm^{-1} respectively). The cell features emerged in these images. The features were selected randomly, and the MIP spectra (2000 to 2300 cm-1) were obtained from these features until sharp peaks manifested, indicating the detection of nitrile groups. The MIP spectra of the selected pixels were obtained by sweeping the QCL laser from 2000 to 2300 cm^{-1} at the speed of 50 cm^{-1}/s and the data points were recorded by a lock-in amplifier with a time constant of 20 ms. The spectra undergo smoothing by Savitzky-Golay method using Origin. It turned out that, for the same molecules, the wavenumbers of C≡N in the cells shift compared to those in DMSO (Figure 2d), likely due to the Stark effect[32]. Thus, the cell morphologies shown at 2205 and 2221 cm^{-1} correspond to the IR absorption of water in the silence-window. So, the IR spectrum of water absorbance background from 2000 to 2300 cm^{-1} was collected by pinpointing to a blank area in the FOV. The pinpointed spectra of C≡N were subtracted by the spectrum of water to give the final pinpointed MIP spectra of C≡N in cells. The data was plotted via GraphPad Prism 8 or Microsoft 365 Excel.

MIP imaging in cell-silent window and water background subtraction:

All samples were imaged under a counter-propagating MIP microscope under the following condition: IR frequency: 1 MHz; IR power: 5–18 mW (depends on wavenumber); Probe beam: 20 mW; IR pulse width: 50 ns; Pixel dual time: 4 μs. A weak and broad-band MIP signal from the water absorption in the silent-window (2000–2300 cm^{-1}) was observed. To remove the water background, two consecutive frames at the peak of C≡N of products and 2080 cm^{-1} (water IR absorbance) or at the peak of C≡N of substrates and 2040 cm^{-1} (water IR absorbance) were collected, respectively. The fast (4 μs/pixel or 1 s/frame for 500×500) imaging speed of MIP microscope endows minimum sample moves between two consecutive frames, as well as little subtraction artifact. This statement is supported by the observation that the cells in blank control groups exhibit no signal after subtraction (Supplementary Figure 8a). Thus, all MIP images collected at the peak of C≡N of products were subtracted by those collected at 2080 cm^{-1} to remove the water background and to generate the final images. Moreover, all MIP images collected at the peak of C≡N of substrates were subtracted by those collected at 2040 cm^{-1} to remove the water background and to generate the final images. The selection of 2080 and 2040 cm^{-1} is based on that the MIP signal intensity in the blank area of a FOV at these wavenumbers is equal to the MIP signal intensity at the wavenumbers of C≡N of products and substrates in the same blank region, respectively.

Determination of probe solubility:

To assess probe solubility, **Casp-CN(S)** and **Phos-CN(S)** were mixed into PBS at a final concentration of 1 mM. After being vortexed for 10 min, the mixtures were filtered through a 0.22 μm syringe filter. By measuring the UV absorbance of the filtrate and subsequent comparison to a standard curve, we found that the concentrations of both probes in filtrates were 1 mM, indicating that the maximum solubility of the probes exceeds 1 mM in PBS.

This solubility is significantly higher than the working concentration (50 μM). These results confirm that although both **Casp-CN(S)** and **Phos-CN(S)** formed small nanoparticles in PBS at 50 μM, these nanoparticles, like micelles formed by surfactants, can be uniformly dispersed in an aqueous solution.

Image processing:

All images were opened and processed by ImageJ. Colocalization analysis was done by ImageJ using the colocalization threshold and coloc 2 plugin. 3D reconstruction was done by ImageJ using the 3D viewer plugin. The whole cell was selected for quantification of MIP signal in a cell and for colocalization analysis. The data was plotted via GraphPad Prism 8 or Microsoft 365 Excel. All MIP images of nitrile chameleons were 32-bit. All fluorescence images are 8-bit. MIP images of nitrile chameleons were converted to 8-bit upon the comparation to fluorescence images.

Supplementary Material

Refer to Web version on PubMed Central for supplementary material.

Acknowledgements:

This work was supported by R35GM136223 and R33CA261726 to J.X.C., R01CA142746 to B.X., and grant 2023-321163 from Chan Zuckerberg DAF, an advised fund of Silicon Valley Community Foundation.

Data availability:

All data related to the work is available in the article and supplementary information within this paper. The Original data of figures is available in doi:XXXXXXX. Other data is available upon reasonable request to the corresponding author.

References

1. Baruch A, Jeffery DA & Bogyo M Enzyme activity–it's all about image. Trends Cell Biol 14, 29–35 (2004). [PubMed: 14729178]
2. Patel T, Gores GJ & Kaufmann SH The role of proteases during apoptosis. The FASEB Journal 10, 587–597 (1996). [PubMed: 8621058]
3. Zhang J et al. Fluorogenic probes for disease-relevant enzymes. Chem Soc Rev 48, 683–722 (2019). [PubMed: 30520895]
4. Chyan W & Raines RT Enzyme-activated fluorogenic probes for live-cell and in vivo imaging. ACS chemical biology 13, 1810–1823 (2018). [PubMed: 29924581]
5. Xing B, Khanamiryan A & Rao J Cell-permeable near-infrared fluorogenic substrates for imaging β-lactamase activity. Journal of the American Chemical Society 127, 4158–4159 (2005). [PubMed: 15783183]
6. Grimm JB, Heckman LM & Lavis LD The chemistry of small-molecule fluorogenic probes. Progress in molecular biology and translational science 113, 1–34 (2013). [PubMed: 23244787]
7. Kwan DH et al. Self-immobilizing fluorogenic imaging agents of enzyme activity. Angewandte Chemie 123, 314–317 (2011).
8. Johnson DS, Weerapana E & Cravatt BF Strategies for discovering and derisking covalent, irreversible enzyme inhibitors. Future medicinal chemistry 2, 949–964 (2010). [PubMed: 20640225]
9. Noe MC & Gilbert AM Targeted covalent enzyme inhibitors. Annu Rep Med Chem 47, 413–439 (2012).

10. He H et al. Enzymatic noncovalent synthesis. Chem Rev 120, 9994–10078 (2020). [PubMed: 32812754]
11. Zhou J et al. Enzyme-instructed self-assembly for spatiotemporal profiling of the activities of alkaline phosphatases on live cells. Chem 1, 246–263 (2016). [PubMed: 28393126]
12. Liu HW et al. In situ localization of enzyme activity in live cells by a molecular probe releasing a precipitating fluorochrome. Angewandte Chemie International Edition 56, 11788–11792 (2017). [PubMed: 28755456]
13. Gao Y et al. Imaging self-assembly dependent spatial distribution of small molecules in a cellular environment. Langmuir 29, 15191–15200, doi:10.1021/la403457c (2013). [PubMed: 24266765]
14. Zanetti-Domingues LC, Tynan CJ, Rolfe DJ, Clarke DT & Martin-Fernandez M Hydrophobic fluorescent probes introduce artifacts into single molecule tracking experiments due to non-specific binding. PLoS One 8, e74200, doi:10.1371/journal.pone.0074200 (2013). [PubMed: 24066121]
15. Bao K et al. Charge and hydrophobicity effects of NIR fluorophores on bone-specific imaging. Theranostics 5, 609 (2015). [PubMed: 25825600]
16. Kim BJ & Xu B Enzyme-instructed self-assembly for cancer therapy and imaging. Bioconjugate chemistry 31, 492–500 (2020). [PubMed: 31995365]
17. Razgulin A, Ma N & Rao J Strategies for in vivo imaging of enzyme activity: an overview and recent advances. Chem Soc Rev 40, 4186–4216 (2011). [PubMed: 21552609]
18. Hamilton BR et al. Mapping enzyme activity on tissue by functional mass spectrometry imaging. Angewandte Chemie 132, 3883–3886 (2020).
19. Xia Q, Yin J, Guo Z & Cheng J-X Mid-Infrared Photothermal Microscopy: Principle, Instrumentation, and Applications. The Journal of Physical Chemistry B 126, 8597–8613 (2022). [PubMed: 36285985]
20. Bai Y, Yin J & Cheng J-X Bond-selective imaging by optically sensing the mid-infrared photothermal effect. Science Advances 7, eabg1559 (2021). [PubMed: 33990332]
21. Zhang D et al. Depth-resolved mid-infrared photothermal imaging of living cells and organisms with submicrometer spatial resolution. Science advances 2, e1600521 (2016). [PubMed: 27704043]
22. Yin J et al. Video-rate mid-infrared photothermal imaging by single-pulse photothermal detection per pixel. Science Advances 9, eadg8814 (2023). [PubMed: 37315131]
23. Tai F et al. Detecting nitrile-containing small molecules by infrared photothermal microscopy. Analyst 146, 2307–2312 (2021). [PubMed: 33620044]
24. Wei L et al. Super-multiplex vibrational imaging. Nature 544, 465–470 (2017). [PubMed: 28424513]
25. Yin J et al. Nanosecond-resolution photothermal dynamic imaging via MHZ digitization and match filtering. Nature Communications 12, 7097 (2021).
26. Gao Y, Shi J, Yuan D & Xu B Imaging enzyme-triggered self-assembly of small molecules inside live cells. Nature communications 3, 1033 (2012).
27. Yi M et al. Enzyme Responsive Rigid-Rod Aromatics Target “Undruggable” Phosphatases to Kill Cancer Cells in a Mimetic Bone Microenvironment. Journal of the American Chemical Society 144, 13055–13059 (2022). [PubMed: 35849554]
28. Wei L et al. Live-cell imaging of alkyne-tagged small biomolecules by stimulated Raman scattering. Nature methods 11, 410–412 (2014). [PubMed: 24584195]
29. Wang R et al. Aggregation enhanced responsiveness of rationally designed probes to hydrogen sulfide for targeted cancer imaging. Journal of the American Chemical Society 142, 15084–15090 (2020). [PubMed: 32786798]
30. Hanczyc P & Fita P Laser Emission of Thioflavin T Uncovers Protein Aggregation in Amyloid Nucleation Phase. ACS Photonics 8, 2598–2609, doi:10.1021/acsphotonics.1c00082 (2021). [PubMed: 34557567]
31. Zaguri D et al. Kinetic and Thermodynamic Driving Factors in the Assembly of Phenylalanine-Based Modules. ACS Nano 15, 18305–18311, doi:10.1021/acsnano.1c07537 (2021). [PubMed: 34694771]

32. Fried SD & Boxer SG Measuring electric fields and noncovalent interactions using the vibrational Stark effect. Accounts Chem Res 48, 998–1006 (2015).
33. Feng Z et al. Artificial intracellular filaments. Cell Reports Physical Science 1 (2020).
34. Qiu C et al. Advanced strategies for overcoming endosomal/lysosomal barrier in nanodrug delivery. Research 6, 0148 (2023). [PubMed: 37250954]
35. He H, Wang H, Zhou N, Yang D & Xu B Branched peptides for enzymatic supramolecular hydrogelation. Chem Commun 54, 86–89 (2018).
36. Guo J et al. The ratio of hydrogelator to precursor controls the enzymatic hydrogelation of a branched peptide. Soft matter 16, 10101–10105 (2020). [PubMed: 32785414]
37. He H et al. Dynamic continuum of nanoscale peptide assemblies facilitates endocytosis and endosomal escape. Nano letters 21, 4078–4085 (2021). [PubMed: 33939437]
38. Sztiller-Sikorska M, Jakubowska J, Wozniak M, Stasiak M & Czyz M A non-apoptotic function of caspase-3 in pharmacologically-induced differentiation of K562 cells. Brit J Pharmacol 157, 1451–1462 (2009). [PubMed: 19627286]
39. Wilhelm S, Wagner H & Häcker G Activation of caspase-3-like enzymes in non-apoptotic T cells. Eur J Immunol 28, 891–900 (1998). [PubMed: 9541584]
40. Carlile GW, Smith DH & Wiedmann M Caspase-3 has a nonapoptotic function in erythroid maturation. Blood 103, 4310–4316 (2004). [PubMed: 14976035]
41. Zhou J, Du X, Li J, Yamagata N & Xu B Taurine boosts cellular uptake of small D-peptides for enzyme-instructed intracellular molecular self-assembly. Journal of the American Chemical Society 137, 10040–10043 (2015). [PubMed: 26235707]
42. Andrews LD, Zalatan JG & Herschlag D Probing the origins of catalytic discrimination between phosphate and sulfate monoester hydrolysis: comparative analysis of alkaline phosphatase and protein tyrosine phosphatases. Biochemistry 53, 6811–6819, doi:10.1021/bi500765p (2014). [PubMed: 25299936]
43. Li X et al. Introducing D-amino acid or simple glycoside into small peptides to enable supramolecular hydrogelators to resist proteolysis. Langmuir 28, 13512–13517 (2012). [PubMed: 22906360]
44. Torres J et al. Phosphorylation-regulated cleavage of the tumor suppressor PTEN by caspase-3: implications for the control of protein stability and PTEN-protein interactions. J Biol Chem 278, 30652–30660 (2003). [PubMed: 12788938]
45. Hallé M et al. Caspase-3 regulates catalytic activity and scaffolding functions of the protein tyrosine phosphatase PEST, a novel modulator of the apoptotic response. Mol Cell Biol 27, 1172–1190 (2007). [PubMed: 17130234]
46. Gao Y, Shi J, Yuan D & Xu B Imaging enzyme-triggered self-assembly of small molecules inside live cells. Nature Commun. 3, 1–8 (2012).
47. Cai Y et al. Environment-sensitive fluorescent supramolecular nanofibers for imaging applications. Anal Chem 86, 2193–2199 (2014). [PubMed: 24467604]
48. Yang C, Chang J, Gorospe M & Passaniti A Protein tyrosine phosphatase regulation of endothelial cell apoptosis and differentiation. Cell Growth and Differentiation-Publication American Association for Cancer Research 7, 161–172 (1996).
49. Halle M, Tremblay ML & Meng TC Protein tyrosine phosphatases: emerging regulators of apoptosis. Cell Cycle 6, 2773–2781, doi:10.4161/cc.6.22.4926 (2007). [PubMed: 17998804]
50. Sangwan V et al. Protein-tyrosine phosphatase 1B deficiency protects against Fas-induced hepatic failure. J Biol Chem 281, 221–228, doi:10.1074/jbc.M507858200 (2006). [PubMed: 16234234]
51. Van Hoof C & Goris J Phosphatases in apoptosis: to be or not to be, PP2A is in the heart of the question. Biochimica et Biophysica Acta (BBA)-Molecular Cell Research 1640, 97–104 (2003). [PubMed: 12729918]
52. Chen MJ, Dixon JE & Manning G Genomics and evolution of protein phosphatases. Science signaling 10, eaag1796 (2017). [PubMed: 28400531]
53. Brantley SJ et al. Discovery of small molecule inhibitors for the C. elegans caspase CED-3 by high-throughput screening. Biochem Bioph Res Co 491, 773–779 (2017).

54. Stergiou L, Doukoumetzidis K, Sendoel A & Hengartner M The nucleotide excision repair pathway is required for UV-C-induced apoptosis in Caenorhabditis elegans. Cell Death & Differentiation 14, 1129–1138 (2007). [PubMed: 17347667]

55. Fonta C, Negyessy L, Renaud L & Barone P Areal and subcellular localization of the ubiquitous alkaline phosphatase in the primate cerebral cortex: evidence for a role in neurotransmission. Cereb Cortex 14, 595–609, doi:10.1093/cercor/bhh021 (2004). [PubMed: 15054075]

56. Bardet P-L et al. A fluorescent reporter of caspase activity for live imaging. Proceedings of the National Academy of Sciences 105, 13901–13905 (2008).

57. Ye D et al. Bioorthogonal cyclization-mediated in situ self-assembly of small-molecule probes for imaging caspase activity in vivo. Nature chemistry 6, 519–526 (2014).

58. Van de Bittner GC, Bertozzi CR & Chang CJ Strategy for dual-analyte luciferin imaging: in vivo bioluminescence detection of hydrogen peroxide and caspase activity in a murine model of acute inflammation. Journal of the American Chemical Society 135, 1783–1795 (2013). [PubMed: 23347279]

59. Ntziachristos V, Tung C-H, Bremer C & Weissleder R (Nature Publishing Group US New York, 2002).

60. Fujioka H et al. Multicolor activatable Raman probes for simultaneous detection of plural enzyme activities. Journal of the American Chemical Society 142, 20701–20707 (2020). [PubMed: 33225696]

61. Shi L et al. Mid-infrared metabolic imaging with vibrational probes. Nature methods 17, 844–851 (2020). [PubMed: 32601425]

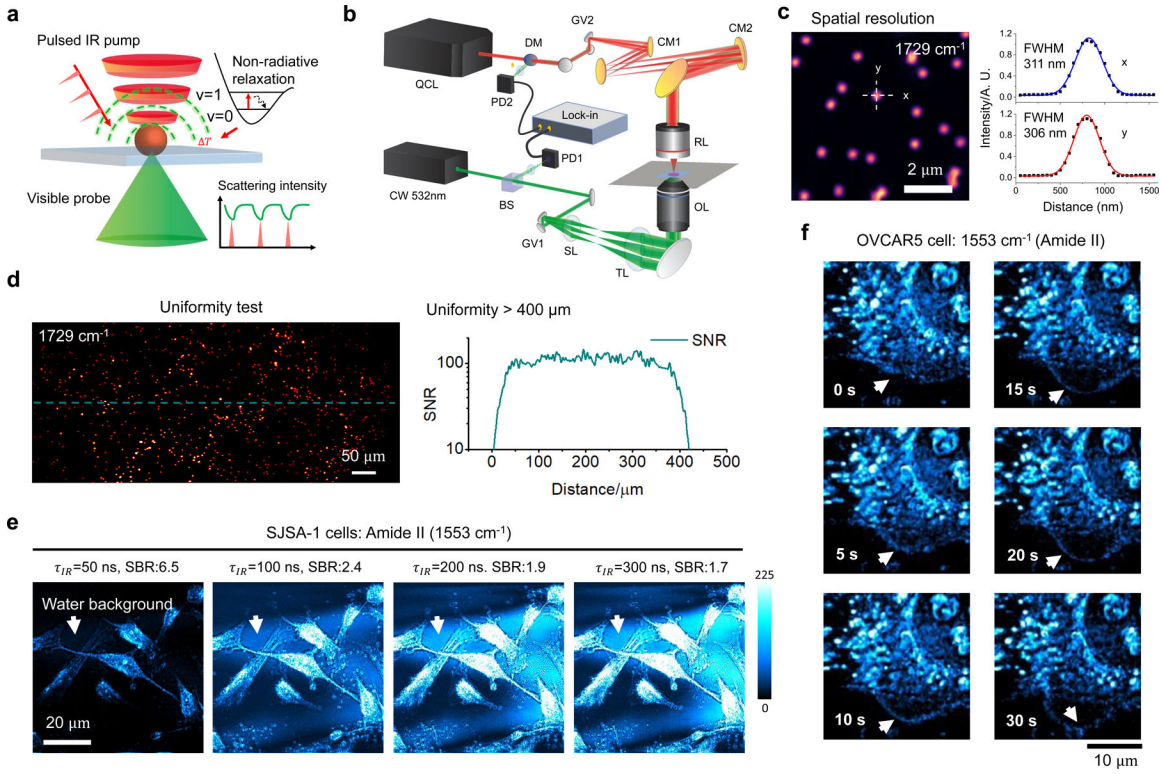

Figure 1. A laser-scan mid-infrared photothermal (MIP) microscope for real-time bond-selective imaging of living cells at 300-nm spatial resolution.

(a) Principle of MIP detection.

(b) Schematic illustration of MIP microscope.

(c) Spatial resolution characterized with 200-nm diameter PMMA particles.

(d) Uniformity characterization by MIP imaging of 500-nm diameter PMMA particles signal to noise ratio (SNR).

(e) MIP imaging of proteins in cancer cells with different IR excitation pulse width.

(f) Live cell MIP imaging of protein dynamics (1553 cm^{-1}, amide II) in cancer cells. All experiments in (c)-(f) were repeated independently for 3 times with similar results.

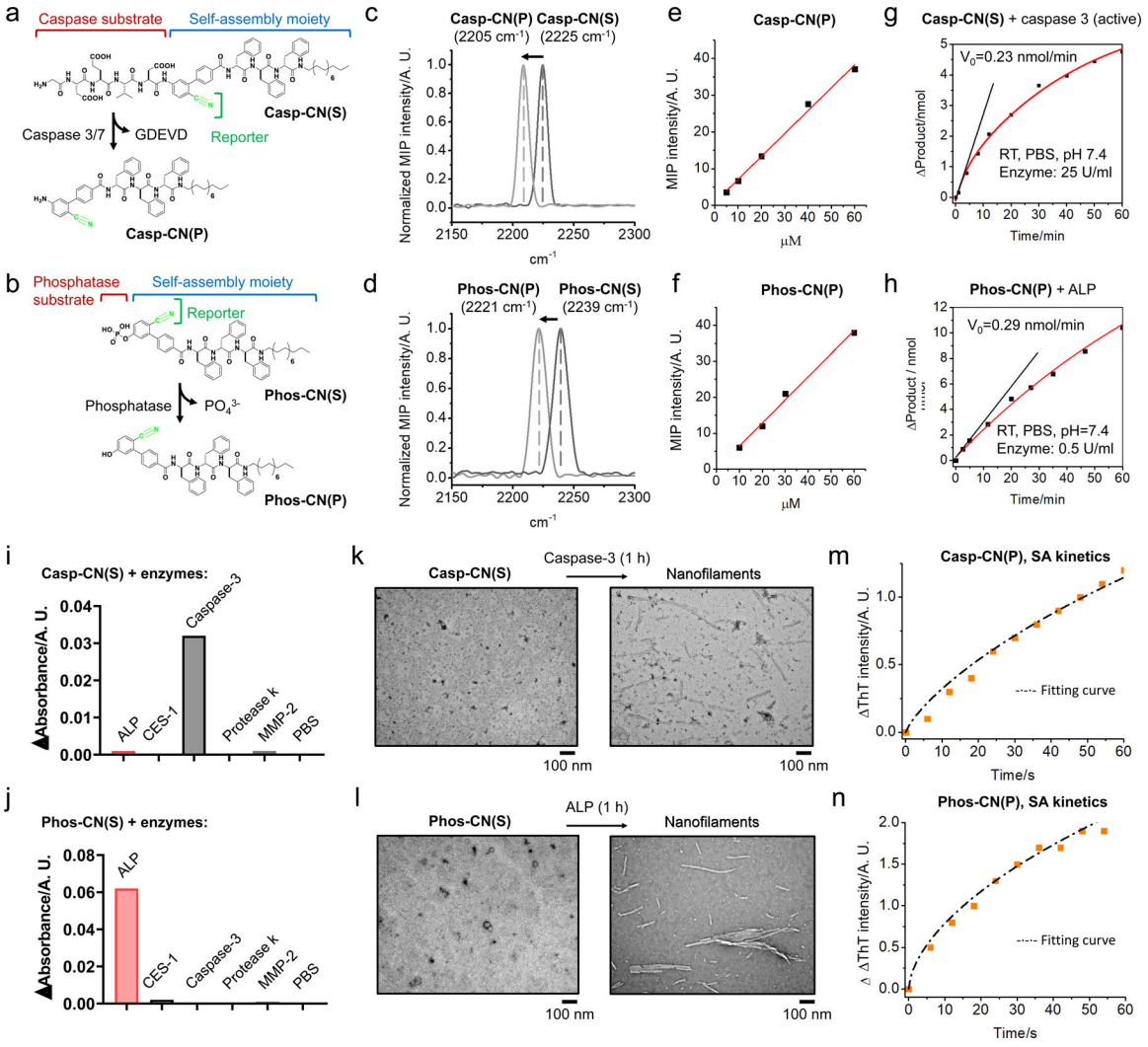

Figure 2. Development of nitrile chameleons for mapping specific enzyme activity.

(a) Molecular structures of **Casp-CN(S)** and the enzymatic product **Casp-CN(P)**.

(b) Molecular structures of **Phos-CN(S)** and the enzymatic product **Phos-CN(P)**.

(c) MIP spectra of **Casp-CN(S)** and the enzymatic product **Casp-CN(P)**, 50 mM in DMSO.

(d) MIP spectra of **Phos-CN(S)** and the enzymatic product **Phos-CN(P)**, 50 mM in DMSO.

(e,f) MIP signal intensity of (e) **Casp-CN(P)** and (f) **Phos-CN(P)** at different concentration concentrations in DMSO.

(g) Time-dependent formation of **Casp-CN(P)** catalyzed by active caspase 3 (25 U/mL).

(h) Time-dependent formation of **Phos-CN(P)** catalyzed by alkaline phosphatase (ALP, 0.5 U/mL)

(I,j) UV absorbance changes in the mixtures of (i) **Casp-CN(S)** or (j) **Phos-CN(S)** with PBS, ALP, caspase-3 (active), carboxylesterase-1 (CES-1), matrix metalloproteinase-2 (MMP-2), and proteinase K.

(k) TEM images of the nano-assemblies formed by **Casp-CN(S)** before and after the addition of active caspase 3 (25 U/mL, 1 h). TEM imaging was repeated independently 3 times with similar results.

(l) TEM images of the nano-assemblies formed by **Phos-CN(S)** before and after the addition of alkaline phosphatase (ALP, 1 U/mL 1 h). TEM imaging was repeated independently 3 times with similar results.
(m,n) Self-assembly (SA) kinetics of enzymatic products (m) **Casp-CN(P)** and (n) **Phos-CN(P)**.

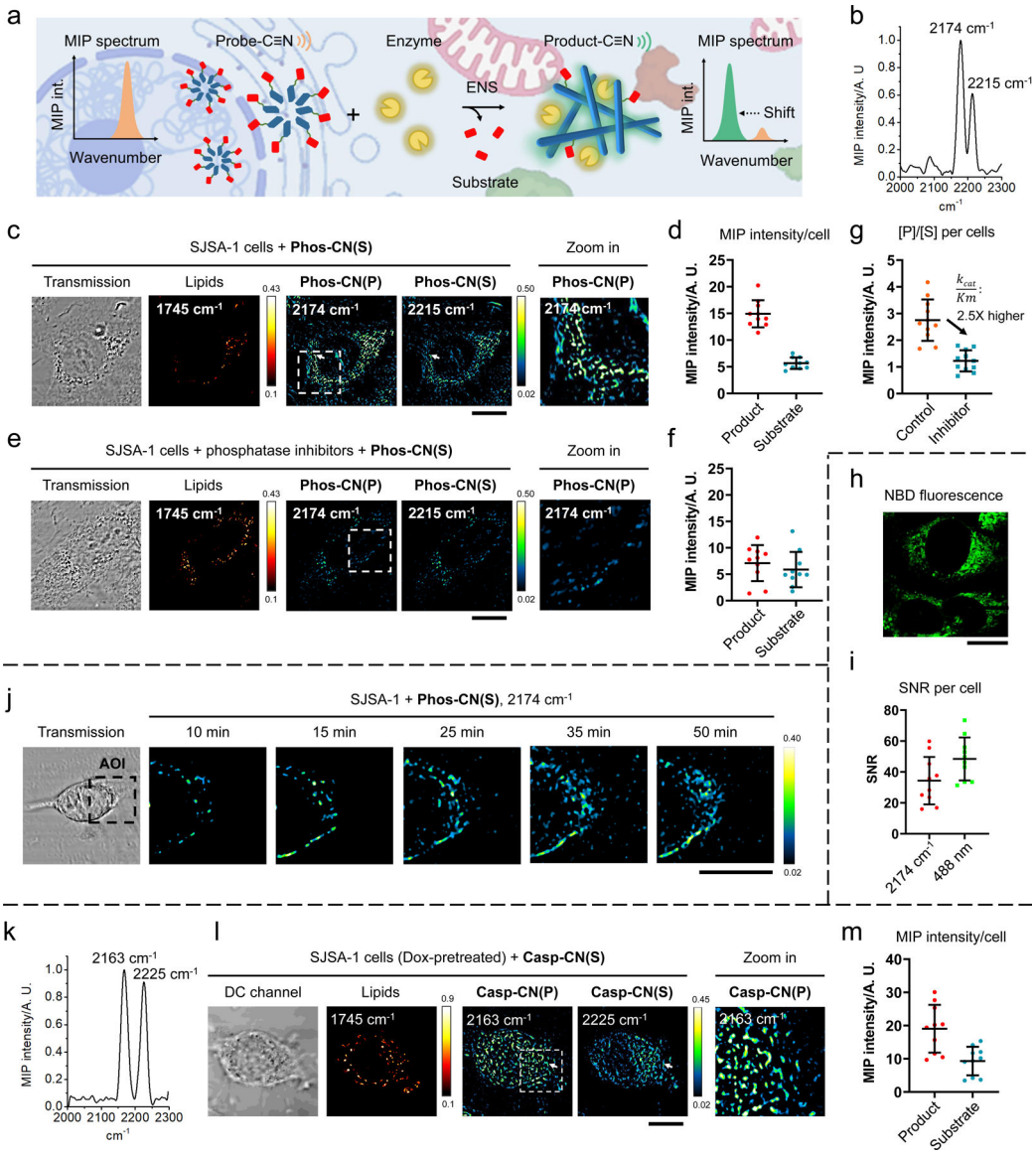

Figure 3. Real-time MIP imaging of nitrile chameleons generates the activity maps of caspase 3/7 and phosphatase in living cells.

(a) Schematic illustration of the principle of enzyme activity mapping by real-time MIP imaging of nitrile chameleons.

(b) Pinpointed MIP spectrum, indicated by arrow in panel c.

(c) MIP images of phosphatase activity profile in living SJSA-1 cells. Scale bar=30 μm

(d) Quantification of MIP signal intensity of **Phos-CN(S)** and **Phos-CN(P)** in cells. n=10 cells. Data are presented as mean±SD.

(e) MIP images of phosphatase activity profile in phosphatase inhibitor-pretreated SJSA-1 cells. Scale bar=30 μm

(f) Quantification of MIP signal intensity of **Phos-CN(S)** and **Phos-CN(P)** in phosphatase inhibitor-pretreated SJSA-1 cells. n=10 cells. Data are presented as mean±SD.

(g) Quantitation of product-to-substrate ratio ([P]/[S]) in the cells from PIC-pretreated and PIC-free groups. n=11 cells. Data are presented as mean±SD.

(h) Confocal fluorescence image of SJSA-1 cells incubated with NBD-label phosphatase activity reporter (**NBD-Phos-CN(S)**, 50 μM, 1h). Scale bar=30 μm

(i) Comparison of SNR between MIP imaging of C≡N (at 2174 cm^{-1}) and fluorescence imaging of NBD in cancer cells. Each dot represents a cell. n=10 cells. Data are presented as mean±SD.

(j) Time-course MIP images of the phosphatase activity as **Phos-CN(S)** (50 μM in PBS, room temperature) was added to cells. Scale bar=30 μm

(k) Pinpoint MIP spectrum, indicated by arrow in panel l

(l) MIP images of caspase 3/7 activity profile in Doxorubicin-pretreated SJSA-1 cells. Scale bar=30 μm

(m) Quantification of MIP intensity of **Casp-CN(S)** and **Casp-CN(P)** in Dox-pretreated cells and the cells from Dox-free control group. n=10 cells. Data are presented as mean±SD.

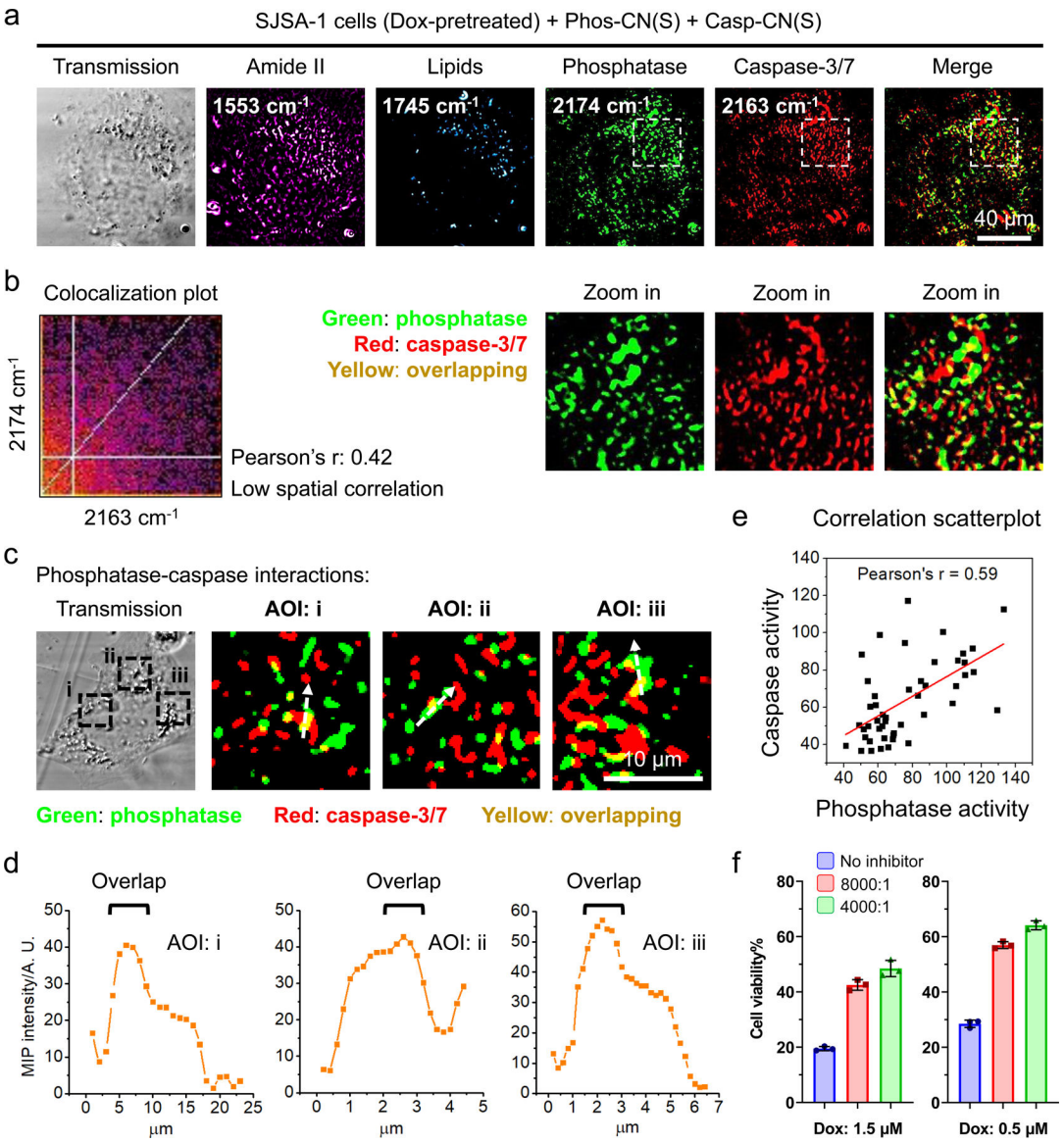

Figure 4. Multicolor MIP imaging of nitrile chameleons in live cancer cells provides evidence of caspase-phosphatase cooperation in apoptosis.

(a) Simultaneous visualization of phosphatase and caspase-3/7 activity profile in Dox-pretreated SJSA-1 cells. Experiment was repeated independently 12 times with similar results.

(b) Colocalization analysis of the mapping in (a).

(c) Spatial interaction between phosphatase and caspase-3/7 in Dox-pretreated SJSA-1 cells. Similar results were observed in 12 independent experiments.

(d) Intensity plot of **Phos-CN(P)** along the arrows in (c).

(e) Correlation scatterplot of caspase-3/7 and phosphatase activity in Dox-pretreated SJSA-1 cells

(f) Cell viability assay of SJSA-1 cells incubated with Dox in the presence and absence of phosphatase inhibitor cocktails. Phosphatase inhibitor cocktails were diluted by 4000

and 8000 times respectively using culture medium. n=3 independent experiments. Data are presented as mean±SD.

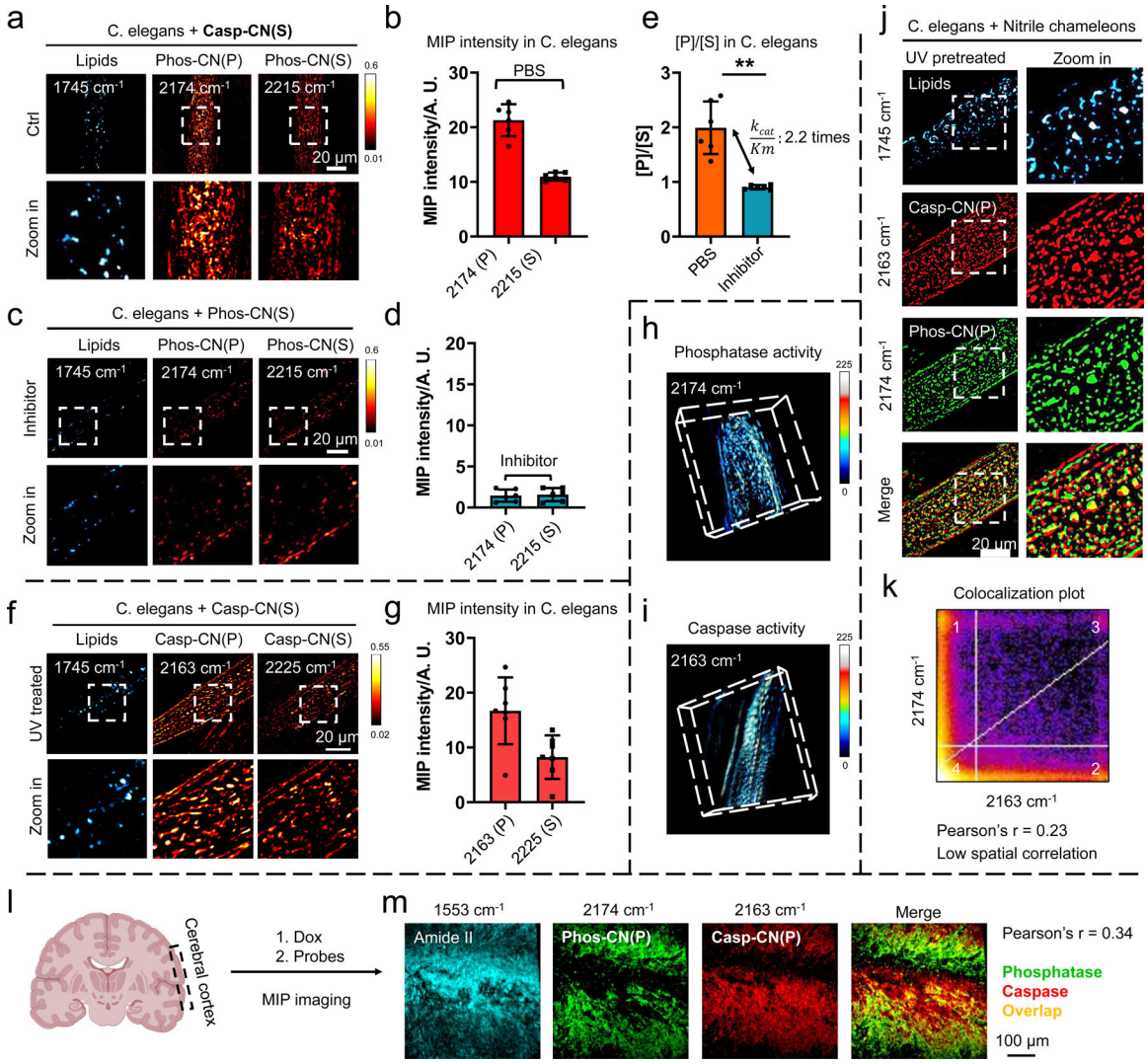

Figure 5. Multicolor MIP imaging of nitrile chameleons generates activity maps of caspase and phosphatase inside C. elegans and brain tissues.

(a) MIP imaging of phosphatase profile in living C. elegans.

(b) Quantification of the MIP signal intensity from **Phos-CN-(P)** and **Phos-CN-(S)** in the inhibitor-free C. elegans. n=6 *C. elegans*. Data are presented as mean±SD.

(c) MIP imaging of phosphatase activity profile in the PIC-pretreated C. elegans.

(d) Quantification of the MIP signal intensity from **Phos-CN-(P)** and **Phos-CN-(S)** in the PIC-pretreated C. elegans. n=6 *C. elegans*. Data are presented as mean±SD.

(e) Statistic of phosphatase [P]/[S] values in the inhibitor-free C. elegans and PIC-pretreated C. elegans. n=6 *C. elegans*. Data are presented as mean±SD. Statistics was performed by paired t-test (two-tailed) without adjustments for multiple comparisons. The p value is 0.0019. ** p≤0.01.

(f) MIP imaging of caspase activity profile in UV-pretreated C. elegans.

(g) Quantification of the MIP signal intensity from **Casp-CN-(P)** and **Casp-CN-(S)** in the UV-pretreated and drug-free C. elegans. n=6 *C. elegans*. Data are presented as mean±SD.

(h,i) 3D reconstruction of (h) phosphatase activity and (i) caspase activity in C. e elegans.

(j) Simultaneous activity mapping of phosphatase and caspase in UV-pretreated C. elegans. The experiment was repeated independently at least 10 times with similar results.
(k) Colocalization analysis of the mapping in (j).
(l,m) Simultaneous mapping of phosphatase and caspase activities in Dox-pretreated (1 μM) mouse cerebral cortex sections. The experiment was repeated independently 10 times with similar results.